Nat. Hazards Earth Syst. Sci. Discuss., 3, 2051–2098, 2015
www.nat-hazards-earth-syst-sci-discuss.net/3/2051/2015/
doi:10.5194/nhessd-3-2051-2015

Natural Hazards and Earth System Sciences
Open Access
Discussions

Analysis of a landslide multi-date inventory in a complex mountain landscape: the Ubaye valley case study

R. Schlögel[1], J.-P. Malet[1], A. Remaître[1], P. Reichenbach[2], and C. Doubre[1]

[1]Institut de Physique du Globe de Strasbourg, UMR7516, Université de Strasbourg/EOST, CNRS, 5 rue René Descartes, 67084 Strasbourg, CEDEX, France
[2]CNR-IRPI, via Madonna Alta 126, 06128 Perugia, Italy

Received: 9 March 2015 – Accepted: 11 March 2015 – Published: 30 March 2015

Correspondence to: R. Schlögel (romy.schlogel@unistra.fr)

Published by Copernicus Publications on behalf of the European Geosciences Union.

Abstract

We propose a methodology (1) to prepare a multi-date landslide inventory for a mountainous area affected by several landslide types with different degrees of activity, and (2) to estimate the temporal occurrence and the intensity of the landslides through the analysis of morphological indicators. The inventory, covering the period 1956–2010, is constructed for the middle section of the Ubaye valley (South French Alps) based on the analysis of multi-source documents (geomorphological maps, historical reports of landslide events, field surveys, series of orthophotographs and SAR satellite images). The uncertainties in the interpretation of the documents and the landslide morphological features are taken into account in relation to the scale of the source documents.

Several morphological indicators are calculated to describe quantitatively the evolution of the landslides (length, area, relative elevation, runout distance). Frequency-area density functions are calculated to estimate the changes in the landslide distributions. A Poisson model is used to estimate the probability of reactivation of the observed landslides. The proposed multi-date inventory and the associated statistics give additional information to the event catalogue managed by local authorities.

1 Introduction

Landslides represent a serious hazard in many areas around the world and include a large variety of types (Varnes, 1978). Landslide inventory maps are important documents to define the spatial distribution of mass movements in a region and to assess landslide susceptibility and hazard (Guzzetti et al., 2012). Geomorphological landslide inventories can provide several categories of information, such as the movement type or the spatial evolution of the landslide extent. If observed, specific geomorphological features (fissures, grabens, ponds, vegetation removal and other morphological changes) underline landslide activity. These descriptors can be used to estimate the temporal and spatial pattern of activity over long time periods (> 50 years).

NHESSD
3, 2051–2098, 2015

For hazard assessment, the spatial and temporal probabilities of landslide occurrence of a certain magnitude have to be evaluated. The spatial distribution of landslides (susceptibility) is primarily controlled by slope morphology, lithology, tectonics and hydrogeological conditions, and by the land cover (Günther et al., 2013; Corominas et al., 2014). The temporal recurrence of landslides is controlled by the occurrence of triggering events (e.g. rainfall, earthquake, rapid snow melt); however, in many cases, the time dimension is difficult to assess due to the lack of historical records (Flageollet, 1999; Sorriso Valvo, 2002; Jaiswal et al., 2011). The magnitude of the events is dependent on the landslide type and several proxies can be used such as the dimensions of the landslide (area, volume, travel distance) or the velocity (Corominas et al., 2014). Frequency–magnitude relationships for different locations and landslide types are frequently used to evaluate the hazard (Malamud et al., 2004; van den Eeckhaut et al., 2007; Schlögel et al., 2011; Florsheim and Nichols, 2013).

The main document for the hazard assessment is the landslide inventory map. Preparing an inventory map is not straightforward and requires experienced geomorphologists trained in the recognition of slope processes and forms (Wills and McCrinck, 2002; van den Eeckhaut et al., 2005). The production of event-based or multi-temporal landslide inventories is hampered by uncertainties associated with the characteristics of the source documents (scale, resolution, time period coverage) as well as with the type and size of the landslides. Optical remote sensing data (e.g. orthophotographs or satellite images) are used to detect landslides by visual analysis or with (semi-)automatic approaches (Barlow et al., 2006; Fiorucci et al., 2011; Mondini et al., 2011; Kurtz et al., 2014). Despite its limited coverage and particular properties, images acquired by Synthetic Aperture Radar (SAR) satellite sensors are also considered as a powerful source of information, mainly for the recognition of slow-moving landslides (Singhroy and Molch, 2004; Zhao et al., 2012). Multi-date landslide inventories (e.g. inventories with temporal information on the landslide extent for more than two dates) over long time periods are not very frequent at the regional scale (Guzzetti et al., 2012)

NHESSD
3, 2051–2098, 2015

because of the complexity to recognize precisely landslide events or typical landslide features in several categories of documents.

The objectives of this work are: (i) to document the evolution of landslides over a period of 55 years exploiting different documents (maps, orthophotographs, satellite images, field surveys, local reports); (ii) to prepare a multi-date landslide inventory map integrating the evolution of morphological descriptors (e.g. landslide boundaries, important geomorphological features underlining landslide activity), and (iii) to estimate the return periods and intensity of the landslides.

The study area corresponds to the middle part of the Ubaye valley (South East France) severely affected by different landslides types (Maquaire et al., 2003) and the investigated time period extents from 1956 to 2010.

2 Study area

The Ubaye valley is located in the South French Alps, an intra-Alpine zone close to the Italian border (Fig. 1a). In the middle section of the valley (e.g. the Barcelonnette Basin), several communities developed throughout the last ten hundreds of years, and the number of inhabitants was around 6000 people in 2012.

The Barcelonnette Basin is a geological window opened in two Eocene crystalline sheet thrusts (Parpaillon and Autapie) overlaying autochthonous black marls (Fig. 1b). Limestone, sandstone, flysch and gypsum constitute most of the rocks within the sheet thrusts; they armed the steepest slopes and crests, ranging from 2500 to 3000 m in elevation. The slopes, with angles varying from 5 to 45°, present an irregular geometry with steep convex planar and hummocky surfaces/profiles. Below the sheet thrusts, the steepest convex slopes (> 35°) are carved in black marl outcrops. The planar slopes (5–15°) are corresponding to moraine deposits of about 10–20 m thickness which are overlaying the black marls. Scree slopes are also covering large areas, especially below the sheet thrust crests with a thickness ranging from 2 to 10 m. The lower parts

NHESSD
3, 2051–2098, 2015

of the slopes and the valley bottom are formed of torrential deposits whose thickness varies from 50 to 200 m.

The climate is controlled by both Mediterranean and mountain influences (Malet et al., 2005b), associating a marked interannual rainfall variability (734 ± 400 mm for the period 1928–2013), significant daily thermal amplitudes (> 20 °C), the occurence of more than 120 days of freezing per year (on average), long dry periods (from May to October) and the occurence of Summer rainstorms (with rainfall intensity up to 60 mm h^{-1} in some cases).

In terms of landcover, forests cover around 40 % of the study area while grasslands and arable lands are present on about 25 and 5 %, respectively; the rest of the terrain is covered by bare soils and urbanized areas (Fig. 1c).

Numerous studies were conducted on the observation, the analysis and the mapping of mass movements (Flageollet et al., 1999; Maquaire et al., 2003; Malet et al., 2005a; Remaître et al., 2005; Thiery, 2007; Razak et al., 2011; Thiery et al., 2014). Several landslide types affect the slopes (Fig. 1a). The landslide typology used in this work, and adapted from Cruden and Varnes (1996) is the following:

- shallow translational landslides (e.g. the Riou-Chanal landslide, South of Uvernet; Fig. 1d);
- deep-seated translational landslides (e.g. the Aiguettes landslide, Fig. 1e; Lopez-Saez et al., 2013);
- deep-seated rotational landslides (e.g. the Pra Bellon landslide, Fig. 1f; Lopez-Saez et al., 2012);
- complex landslides (e.g. the La Valette and Super-Sauze mudslides, Malet et al., 2005a; Travelletti et al., 2014).

To be consistent with the works of Thiery et al. (2007, 2014), the descriptive terms deep-seated and shallow define landslides with depths of respectively more than 6 m and less than 6 m; the depths are estimated from field geomorphological observations.

NHESSD
3, 2051–2098, 2015

3 Materials and methodology

A multi-date inventory map of active, dormant and relict landslides has been compiled at the 1 : 5000 scale for the period 1956–2010. The data sources (Table 1), the methodology of mapping and the structure of the database and the statistical approaches used to investigate the properties of the inventory are described in the following sections.

3.1 Data sources for the multi-date inventory creation

Several documents are used for the multi-date landslide mapping (Fig. 2; Table 1): (i) seven sets of orthophotographs at different spatial resolutions and dates (from 1956 to 2009) acquired by the National Geographical Institute (IGN), (ii) shaded relief and contour lines obtained from an airborne SAR DSM of 2009 (5 m resolution), (iii) mapped elevation contour lines (10 m resolution), (iv) historical reports from the local risk managers (RTM – *Restauration des Terrains en Montagne*) organized as a GIS point-based database, (v) geomorphological landslide inventories for some parts of the study area organised as a GIS polygon-based database (Thiery, 2007), (vi) geological and geomorphological maps (ZERMOS, 1975) providing local information on the unstable slopes, (vii) interferograms of L-band SAR images (Schlögel et al., 2015) used to update the landslide inventory for the years (2007–2010) and to detect unknown landslides, (viii) relief hillshade maps used to detect specific landslide features.

For the first analysis step (Fig. 2), available maps and images (of various scales, spatial resolutions, and formats) were georeferenced (spatial reference system NTF – Lambert Zone III) and ortho-rectified to homogeneise the spatial coverage of the documents. For the second analysis, we performed the 2-D visual interpretation of the orthophotographs complemented with field mapping to update the existing landslide inventory map prepared by Thiery et al. (2007) for the entire Barcelonnette Basin.

Figure 3 indicates the periods for which the landslide events were recorded and mapped: the A_1 inventory provides information on landslide pre-1956; the A_2, A_3, A_4, A_5, A_6 and A_7 inventories provide information on the new and reactivated landslides,

NHESSD
3, 2051–2098, 2015

respectively for the period between 1956 and 1974, between 1974 and 1982, between 1982 and 1995, between 1995 and 2000, between 2000 and 2004 and between 2004 and 2009. The G_{09} geomorphological inventory combines information on the relict (R), dormant (D) and active landslides in 2009. The geomorphological inventories G_{56} and G_{09} are prepared by comparing all the available datasets for the respective dates (Fig. 4); the inventory of active landslides (A_1 to A_7) are created by the visual interpretation of the differences observed for the period being studied, and integrates derived parameters such as a vegetation index and an uncertainty index (Figs. 5 and 6). The multi-date inventory of 2009 is represented in Fig. 7a; the landslides detected by InSAR are indicated in Fig. 7b.

3.1.1 Creation of the landslide inventories from the analysis of maps, orthophotographs and historical reports

The GIS polygon-based landslide inventory of 2004 (Thiery, 2007; Table 1) was used as base document to prepare the inventory maps for the years 1956, 1974, 1982, 1995, 2000 and 2009. The landscape interpretation was performed primarily on the orthophotographs while the geomorphological maps available for intermediate dates (1975, 1989 and 2001) were considered as a secondary source of information. For some landslides, historical reports were available and used to interpret the landslide evolution (Stien, 2001). An example of the maps is presented in Fig. 4 for the Pra-Bellon landslide. Comparison of different geomorphological maps (Fig. 4a–c) with the recent orthophotograph of 2009 (Fig. 4d) allows the interpretation of the landslide evolution.

The time series of orthophotographs is used to detect landslide reactivations for the preparation of the multi-date inventory (see Figs. 5a and 6a). Field surveys were conducted in order to (1) validate the visual recognition of the mapped landslides and (2) complete the database for some descriptors, especially the degree of activity. As geomorphological features left by landslides may not be recognized by traditional methods, as they are often hidden or erased by erosion, vegetation, urbanization and other anthropic actions, the update of the landslide inventory has been increased by the

NHESSD
3, 2051–2098, 2015

analysis of L-band SAR interferograms for the recent years (2007–2010); these interferograms were also used to recognize possible other unstable slopes.

3.1.2 Completion of the 2009 geomorphological inventory with L-band SAR interferograms

Synthetic Aperture Radar Interferometry (InSAR) is an active remote sensing technique using two or more SAR images acquired at different time. The SAR interferograms are the images formed by the difference of a pair of coregistered SAR phase images allowing the generation of deformation maps for the detection and mapping of ground surface changes (Hanssen, 2001). SAR interferograms have been widely used for landslide detection, mapping and monitoring over the last decade (Canuti et al., 2004; Metternich et al., 2005; Colescanti and Wasowski, 2006; Lu et al., 2012) mainly on the basis of Persistent Scatterers (PS-InSAR) techniques for the detection of extremely slow-moving landslides in urbanized areas. As this latter technique is hardly applicable in rural and mountainous environments without corner reflectors, we used a traditional Differential InSAR (D-InSAR) technique (Massonet and Feigl, 1998; Rosen et al., 2000; Cascini et al., 2009).

For the Ubaye valley, only ascending pass ALOS/PALSAR images are available, limiting the coverage of the territory to 60 % because of layover and slope portions hidden by the relief (Fig. 2; Cascini et al., 2009). The interpretable slope portions are those oriented to the N, NW, W, SW and S as well as all the slopes with topographic angles lower than 10°. Further, according to our time series of SAR images, the ambiguity of phase measurements limits the tracking to displacement rates lower than 5.9 cm for periods of 46 days.

The methodology used to process the SAR images with ROI_PAC and NSBAS algorithms (Rosen et al., 2004; Doin et al., 2011) is described in Schlögel et al. (2015). In this work, the SAR interferograms and the deformation maps are used at a regional scale in order to update the geomorphological inventory and detect landslides occurring between 2007 and 2010 (Figs. 2, 3 and 6b).

NHESSD
3, 2051–2098, 2015

Specific spatial arrangements of wrapped phase values are identified in the interferograms. Examples are presented in Fig. 6b. In this case, the spatial arrangement of phase values possibly corresponding to a landslide signal is a circular footprint with a progressive phase difference change. For slow-moving landslides, fringes can be determined (Fig. 6b) and displacement rates are estimated for different time periods (Fig. 6c). For fast-moving landslides, only the presence of a deforming slope is determined on the basis of speckles looking like noise (example of the landslide to the NE in Fig. 6b).

340 SAR signals corresponding to possible landslides were identified on nine interferograms covering the period 2007–2010. These signatures were inspected by a field survey in 2012. The field survey pointed out that some of the SAR signals corresponded to changes in the soil surface properties, such as new infrastructures, cultivated crops or harvested forests. Finally, 110 SAR signals correspond to landslide events (Fig. 7b) and are integrated in the geomorphological inventory of 2009 (Fig. 7b); the others SAR signals correspond to other ground deformation such as rockfalls, sackungs and gully erosion. The boundaries of the landslides detected by SAR interferograms were adjusted according to the morphology of the slope and the observations of the orthophotographs (Fig. 6b).

3.2 Structure of the database and attributes of the multi-date inventory

The landslide information stored in the database is related to (1) new failures triggered between the considered dates, and (2) landslide reactivations identified in the landscape either as a change in landslide size (retrogression of the main scarp, enlargement, downhill progression of the material; Fig. 6a) or as internal deformation (creation of secondary scarps and lobes, changes in the soil surface state). The landslide database combines several descriptors (Table 2):

NHESSD
3, 2051–2098, 2015

– typological descriptors, divided in four categories according to the predominant movement and/or material (shallow translational slide, deep-seated translational slide, rotational slide and mudslide);

– morphological descriptors, including attributes such as (1) the landslide size (area and perimeter), (2) the elevation difference between the lowest and the highest point of the landslide body, (3) the runout distance and the angle of reach (Corominas, 1996) between the landslide crown and the landslide toe;

– kinematic descriptors, including attributes such as (1) the degree of activity, adapted from four age classes proposed by McCalpin et al. (1984) and reclassified into three categories (a – relict landslide when the landslide is still visible in the landscape but shows no morphological evidences of deformation, b – dormant landslide when the landslide exhibits very small displacements in the range of $mm\,yr^{-1}$ and no obvious morphological changes, and c – active landslides when the displacement rates are in the range of $cm\,yr^{-1}$ and when significant changes of the sub-surface morphology are observed; Fig. 5a), (2) the average displacement rate of the landslide evaluated from the spatial evolution of the landslide boundaries, and (3) a vegetation index which describes the state of the vegetation cover and is used as a proxy of landslide activity. The vegetation index is qualitative and based on the interpretation of observed changes in vegetation density on the orthophotographs. It has to be noted that the reactivated landslides are represented in each inventory by polygons with the same shape or size (corresponding to an internal reactivation) or with a change in shape and size (corresponding to an upslope/downslope development or to a widening);

– interpretation descriptors, defined by an uncertainty index qualifying the degree of uncertainty in landslide recognition. This index is qualified assuming several criteria depending on the source documents (quality, spatial resolution), the landslide type (e.g. deep-seated or shallow) and the terrain conditions (e.g. forested area, grassland...). Indeed, forest harvesting, ploughed lands or new infrastruc-

NHESSD
3, 2051–2098, 2015

tures may confuse the visual interpretation by the expert. Two levels of uncertainty are defined for the image interpretation: reliable (when landslide reactivations or new landslides are clearly visible by the expert; Fig. 5a) and supposed (when the interpretation is questionable assuming the criteria; Fig. 5b).

These descriptors are computed for each time interval. Further information on the lithology, surficial formation and land cover of the source and the deposition areas are integrated.

3.3 Analysis of the multi-date inventory

Several descriptive statistics and indicators are calculated to explore the database and evaluate landslide intensity and return periods.

3.3.1 Calculation of landslide density

Landslide density maps are prepared to quantify the spatial abundance of landslides (Campbell, 1973; Wright et al., 1974; DeGraff and Canuti, 1988). Landslide density is the proportion of landslide surfaces per mapping units and is computed with Eq. (1):

$$D_{\mathrm{L}} = \frac{A_{\mathrm{L}}}{A_{\mathrm{M}}}, \quad 0 \leq D_{\mathrm{L}} \leq 1 \tag{1}$$

where, A_{M} is the area of the mapping unit and A_{L} is the landslide cumulated surface in the mapping unit. Density is calculated by counting the slope portion affected by active landslides for the period 1956–2009. In our case, the analysis is performed for a 250 m grid size (corresponding to a surface of 62 500 m^2). The threshold used to consider a grid cell affected by a landslide is the presence of a landslide for a surface larger than 250 m^2 (e.g. 0.04 %). The landslide density is expressed in four classes:]0–0.3[; [0.3–0.5[; [0.5–0.7[; [0.7–1.0].

NHESSD
3, 2051–2098, 2015

3.3.2 Calculation of landslide descriptive statistics

Descriptive statistics are calculated for the geomorphological inventory (combining R, D and G_{56} for 1956; G_{09} for 2009; Table 3). The age of relict (R) and dormant (D) landslides is unknown, but the oldest and largest failures are believed to be from the Holocene period (Jorda, 1980). No reactivation of these landslides has been recorded over the last 60 years. For the active landslides, the evolution of morphological descriptors used as proxies of landslide mobility between 1956 and 2009 is presented for the inventories G_{56} and G_{09}. For the G_{56} inventory, the date of landslide triggering is unknown but these landslides became active at least once between 1956 and 2009. For the G_{09} inventory, both the new and reactivated landslides between 1956 and 2009 are considered (Table 4). A landslide activation correspond either to an internal morphological change within the landslide boundary, or an enlargement of the landslide size (Fig. 4a). The average number of landslide events and areas affecting the study area per year is presented in Table 4.

3.3.3 Calculation of frequency-area density functions

Landslide frequency-area distributions are calculated to compare the landslide distributions for several time periods and morphological sub-units. Two size distribution models were proposed in the literature: (1) the Double Pareto distribution (Stark and Hovius, 2001) defined by a positive and a negative power scaling, and (2) the Inverse Gamma distribution (Malamud et al., 2004) defined by a power-law decay for medium and large landslides and an exponential rollover for small landslides. According to best-fit criteria on our data, we choose a maximum-likelihood fit of the simplified version of the Double Pareto (DPS) distribution defined by Eq. (2):

$$\mathrm{pdf}(x|\alpha,\beta,t) = \frac{\beta(t/\alpha)}{(1+(x/t)^{-\alpha})^{(1+(\beta/\alpha))}(x^{(\alpha+1)})} \quad (2)$$

NHESSD
3, 2051–2098, 2015

where α controls the slope of the distribution for high values tail, β controls the slope for low values, and t controls the position of the maximum of the distribution function (rollover). The webtool developed by Rossi et al. (2012) was used to estimate the DPS distributions of the landslide area directly from the landslide inventory maps. Different frequency density functions were calculated considering the lithology of the landslide source area (marls, moraine, limestones/sandstones/screes), the morphological sub-units (northern zone, southern zone) and the degree of activity (dormant landslides, active landslides in 1956 and 2009; D, G_{56} and G_{09}, respectively in Table 3).

3.3.4 Calculation of landslide time recurrence

The Poisson distribution is a discrete distribution function used for characterizing the temporal occurrence of landslides. The probability of experiencing n landslides during time t is calculated with Eq. (3):

$$P[N_L(t) = n] = P_t = e^{(-\lambda t)} \frac{(\lambda t)^n}{n!} \quad \text{with } n = 0, 1, 2, \ldots \tag{3}$$

where λ is the estimated average rate of landslide occurrence, which corresponds to $1/\mu$, with μ the estimated mean recurrence interval between successive failure events. The model parameters λ and μ are usually obtained from an historical catalogue of landslide events or from a multi-date landslide inventory map. In our multi-date inventory, λ corresponds to the number of landslide recorded in the study area divided by the period considered (e.g. 10 landslides in 53 years = 0.189 landslide yr^{-1}) while μ is the mean time between two successive landslides (53 years with 10 landslides = 5.3 years).

4 Results

The 2009 (G_{09}) and 1956 (G_{56}) geomorphological inventories are used to create the density maps. The two inventories are also used to estimate the size evolution and

NHESSD
3, 2051–2098, 2015

the mobility of active landslides in comparison to relict (R) and dormant (D) landslides. The angle of reach (as a proxy of landslide mobility) and the frequency-area functions are calculated for the different landslide types for the G_9 inventory and compared to the inventory of dormant landslides and the G_{56} inventory. Finally, landslide activity and temporal occurrences are calculated on the basis of the period considered knowing the precise year of (re)-activations (e.g. A_2, A_3, A_4, A_5, A_6 and A_7).

4.1 Analysis of landslide density

This section compares the geomorphological inventory of active landslides observed in 2009 (G_{09}) to the 1956 geomorphological inventory (G_{56}) in terms of landslide extension and location (Table 3).

The density of active landslides in Ubaye is ca. 2.6 landslides km^{-2} (for a total area of 235 km^2). The percentage of deep-seated rotational and deep-seated/shallow translational slides (Table 3) affecting an area is represented on the basis of grid cells of 250 m (Fig. 8a and b). For the analysis, we sub-divided the territory in three morphological units (Fig. 8) delimited in the N/S direction by the Ubaye River (zone 1 to the North, zone 2 to the South) in the W/E direction by the Riou-Versant torrent (zone 3; Fig. 8). High density of translational slides is observed in the zone 1 and to the North of zone 3. In zone 2, all the landslides are distributed homogeneously (Fig. 8a and b). Their average size is around 20 755 m^2 in zone 1, 12 855 m^2 in zone 2 and 10 975 m^2 in zone 3. Deep-seated rotational slides are less present in zone 1 and rarely observed to the East of the Riou-Versant (Fig. 7b). Their average size is around 85 700 m^2 in zone 1, 25 420 m^2 in zone 2 and 109 500 m^2 in zone 3. The landslide average area is almost ten times larger for rotational slides than for translational slides in zone 3. The slopes orientated to the West are more affected by landslides (i.e. mean slope orientations of 220 and 226°; Fig. 8a and b).

Figure 9a indicates that the majority of the slopes oriented to the N, NW and W is affected by landslides, suggesting a dependence with longer persistence of snow cover on these slopes in winter and early spring. Correlation between the landslide

NHESSD
3, 2051–2098, 2015

occurrences and the land cover highlights that more than 60 % of the active landslides are under forest.

4.2 Analysis of landslide evolution

This section describes the landslide geometrical parameters in time for both the relict, dormant and active landslides (R, D, and G_{09}; Table 3). In 2009, the study area is affected by 788 slides corresponding to an average density of ca. 3.4 landslides km^{-2}. 59 slides are relict, 115 slides are dormant and 614 slides are considered as active. In terms of affected surfaces, the relict, dormant and active slides correspond to respectively 7.1, 5.8 and 7.1 % of the surface of the study area (Table 3). The dormant landslides are less numerous but are covering large parts of the study area. The active landslides cover a total area of around 16.6 km^2 (Fig. 9b). The active landslides range in size from. 100 to 140 000 m^2; the average size of the active landslides exhibit a surface of 28 500 m^2 (Fig. 9c). Among the active landslides, the rotational slides are more represented in surface than in number, meaning that they are, on average, larger than the shallow and deep translational landslides (Fig. 9d).

The sizes of the active landslides in 2009 and 1956 (G_{09}; G_{56}; Table 3) are compared. From 1956 to 2009, 102 new landslides are observed corresponding to a surface increase of 2.9 km^2 (1.3 % of the area). The analysis of the elevation differences (Table 2) for the landslides in 1956 and in 2009 indicates small differences, in the range between 20 and 100 m, with an average of ca. 50 m (Fig. 10a). For the runout distances (whatever the landslide type), the distribution is in the range between 10 and more than 2000 m but most of the distances are in the range between 50 and 200 m (Fig. 10b). Figure 9c indicates that the angles of reach are in the range 15–25° for the rotational slides, in the range 12–35° (with a scattered distribution) for the deep translational slides and in the range 30–40° for the shallow translational slides. These values are consistent with the geomorphological features associated to these landslide types.

NHESSD
3, 2051–2098, 2015

4.3 Landslide magnitude: frequency-area distribution

The multi-date landslide inventory was prepared with heterogeneous multi-source data at different resolutions and scales. The landslide inventories are compared with the assumption that the heterogeneity of the dataset and the interpretation rules used for mapping the landslide do no impact the landslide frequency-area distribution. Frequency-area density functions were calculated by taking into account different landslide subsets (Fig. 11): (i) the geomorphological inventory of 2009 (G_{09}; Table 3) classified according to the lithology and, (ii) the geomorphological inventory of 2009 (G_{09}; Table 3) classified according to the morphology; and (iii) the multi-date inventory classified according to landslide activity (D, G_{56} and G_{09}; Table 3).

The frequency-area distributions indicate the presence of only a few very small landslides meaning that some of the landslides are omitted in the database because of their size. The frequency density for medium and large landslides follows a negative power law trend. The α values are 0.62 ± 0.04 (for weathered marls) and 0.57 ± 0.01 (for limestones, sandstones and screes; Fig. 11a) meaning that large events can occur in both lithologies but are expected to be smaller in the weathered marls. The α values are different for the northern area (0.51 ± 0.03) than for the southern area (0.86 ± 0.03; Fig. 11b). It indicates that the landslides are larger in the northern area explained because of specific geomorphological conditions (higher number of steep slopes, presence of the thrust sheets); however, the frequency-area distribution is dependent of the number of events and three very large landslides (Pra Bellon, Les Aiguettes and La Valette) are observed in this unit biasing the calculation. In the southern area, the β values are higher according to the frequency of the small landslides but the distribution is scattered with high values of SD up to ± 0.73. Finally, the frequency-area distribution of the dormant landslides shows a completely different trend than the active landslide because of their large size with a disappearance of the rollover (Fig. 11c). The high variation of β values (1.17 ± 0.12 to 4.49 ± 0.73) indicates the difficulty to map all the small events, especially over the past years, and thus, their underestimation (Guzzetti

NHESSD
3, 2051–2098, 2015

et al., 2002). Despite these limitations, a rollover is observed for the smallest landslides, which are more frequent around 480 m^2 in 1956 (G_{56}) and around 520 m^2 in 2009 (G_{09}).

4.4 Return periods of landslide events: temporal probability assessment

A simple approach to estimate the temporal probability of landslide reactivation is to calculate how many times a portion of the territory is affected by landslides for a given period of time. The exceedance probability of having one or more landslides in each grid-cell (250 m × 250 m) is computed by (i) ascertaining the mean recurrence interval of landslides in each mapping unit (from 1956 to 2009), (ii) assuming that the rate of slope failures remains the same for the future, and (iii) using a Poisson probability model (Crovelli, 2000; Guzzetti et al., 2003, 2005). The landslide recurrence is calculated per grid-cell on the basis of the observed rate of landslide occurrence for the period 1956–2009. Knowing the recurrence time between successive failures for this period, the exceedance probability of landslide reactivation is estimated for four return periods from 5 to 50 years (Fig. 12). For a return period of 10 years, high probability of landslide reactivation is expected to the NW of the area, in relation to the numerous reactivations of the, Pra Bellon, Les Aiguettes and La Valette landslides over the last 6 years. Table 5 indicates the number, area and percentage of cells for different temporal probabilities and return periods. Five probability classes are considered to highlight the evolution of landslide reactivation over time. It shows that in the next 50 years, almost 60 % of the territory already affected by landslides has a probability higher than 0.8 to be reactivated (Fig. 12).

NHESSD
3, 2051–2098, 2015

4.5 Periods of landslide activity and identification of landslide triggering events

4.5.1 Analysis of the period 1850–2010

The periods of landslide activity identified from dendrogeomorphic information (Lopez-Saez et al., 2011, 2012, 2013; Fig. 13a–c) are compared to the landslide catalogues collected by the authorities (RTM and BRGM; Fig. 12d) since 1850. The dendrogeomorphological information was collected only at some unstable slopes (Aiguettes, Pra Bellon and Bois Noir landslides; Fig. 1e and f) while the event catalogue covers the complete study area. Periods (years) of landslide activity are identified from the comparison of the landslide catalogues. Thirty one and ten periods with increased landslide activity are respectively identified in two and three datasets (arrows in Fig. 13). From the dendrogeomorphological analysis, Lopez-Saez et al. (2013) identified twelve major reactivations for the Aiguettes landslide (i.e. in 1898, 1904, 1911, 1916, 1936, 1961, 1971, 1977, 1979, 1996, 1998, and 2004). Considering the timing of annual tree ring formation at Bois Noir, landsliding is likely to have occurred in 1874–1875, 1896–1897, 1946–1947, 1992–1993, and 2003–2004 (Lopez-Saez et al., 2011). According to Lopez-Saez et al. (2012), the Pra Bellon landslide had no relevant reactivation for the period 1980–1990, while the La Valette landslide has been triggered in 1982 and major failures were observed at Super-Sauze between 1978 and 1982 (Flageollet et al., 1999; Malet, 2003). Figure 13 indicates that many landsliding events were recorded at Bois Noir landslide for the year 2004 but only a few landslides are recorded elsewhere in the region. This proves the difficulty to extrapolate local information from specific slopes to the valley scale.

4.5.2 Analysis of the period 1956–2009

Table 4 indicates the number, area and density properties of the new and the reactivated landslides for the period 1956–2009. On the whole territory, only a few new

NHESSD
3, 2051–2098, 2015

landslides (from 1. to 4.4 landslides year^{-1}) occurred while landslide reactivations are numerous (from 7.3 to 33.1 landslides year^{-1}). The evolution of the area and number of active landslides from 1956 to 2009 (A_2, A_3, A_4, A_5, A_6 and A_7; Table 4) is presented in Figs. 14 and 15a, respectively. For the entire period (A_2–A_7), the new landslides are represented in black, the reactivated landslides defined by changes in size are in dark grey and the reactivated landslides defined by internal deformation are in grey; the supposed active landslides (uncertainty index equals to 2) are shown in dotted lines. Figure 15a points out that the period A_3 (between 1974 and 1982) recorded more new and reactivated landslides than the other periods with respectively 33 and 4 events per year. In comparison, periods A_2 and A_4 are less affected by landslide events with less than 2 new landslides or 12 reactivations per year. After 1995, more landslides were observed. A peak of landslide activity (Fig. 15a) is observed in terms of number of events for the period G, but this is not observed in terms of evolution of landslide sizes (Fig. 14). For the period 1995–2009 (A_5, A_6 and A_7), the number of active landslides is roughly the same while an increase of areas affected by landslides from 2004 to 2009 (A_7) is recorded.

4.5.3 Relationships between landslide activity and triggering events

This section aims at analysing the various landslide catalogues and identifying possible relations with triggering events. For the study area, rainfall cumulated thresholds and rainfall intensity thresholds are established for the occurrence of debris flow events (Flageollet et al., 1999; Remaître et al., 2015); for shallow and deep-seated landslides, the definition of rainfall thresholds is difficult.

The periods of landslide activity identified in the geomorphological inventories (A_2, A_3, A_4, A_5, A_6 and A_7; Table 4), the dendrogeomorphologic observations (Fig. 13a–c) and the landslide historical catalogue (Fig. 13d) are compared to the average annual rainfall (712 ± 152 mm) for the period 1956–2010 (Fig. 15). Nine periods of landslide activity (represented by arrows in Fig. 13) are identified in the three datasets.

NHESSD
3, 2051–2098, 2015

At the annual scale, the landslide–rainfall relationship is not straightforward; for instance, for the periods of landslide activity before 1970, yearly rainfall amounts of 900 to 1000 mm are observed, while for the periods of landslide activity after 1970, yearly rainfall amounts of 750 mm are observed (Fig. 15). Conversely, periods of landslide activity recorded in the catalogues may also correspond to relatively dry periods such as for the year 1964 and the periods from 1982 to 1990.

For the period 1956–1972, rainfall amounts higher than 1000 mm (e.g. respectively 1075 and 1028 mm) are recorded but landslides occurred only during two years (1960, 1963) during this period (on the basis of the landslide historical catalogue and the dendrogeomorpholgical observations) and evidences of landslides are not identified from the visual interpretation of the orthophotographs. This might be explained by the effect of the quality (black and white) and resolution of the oldest orthophotographs (Fig. 14). The period 1974–1982 is affected by successive years with annual rainfall amounts (791 ± 179 mm; Fig. 15c) higher than the normal. Many (re)-activations were observed during this period from the visual interpretation of the orthophotographs (Fig. 15a); surprisingly, only a small amount of landslides are recorded by the local risk managers. The period 1982–1995 is affected by successive years with annual rainfall amounts (690 ± 124 mm) lower than the normal. Few landslide (re)-activations are observed in the orthophotographs while several are recorded by the local risk managers. From 1995 to 2000, the average annual rainfall amounts is close to the normal (802 ± 112 mm) and only a few landslides are recorded in the three databases. Between 2000 and 2004 and 2004 and 2009, the annual rainfall amounts are lower than the normal (respectively 626 ± 143 mm and 568 ± 131 mm), and no landslides are identified in the databases. Further, for the year 2003, more than three events are identified in the dendrogeomorphic observations while no event was recorded in the historical event catalogue (Fig. 15). This indicates that the historical catalogue is not complete and that the geomorphological inventory, even if it is time-consuming to prepare and that the interpretation is dependent on the experience of the geoscientist, give access to useful additional information. However, an overestimation of landslide (re)-activation may also

NHESSD
3, 2051–2098, 2015

be possible as the quality and resolution of the orthophotographs acquired after 2000 are better.

As the relationships between the periods of landslide events and the cumulated annual rainfall amounts are not straightforward, the relationships between the cumulated rainfall amounts for the winter months (January, February and March) are analysed. At first order, a threshold can be established in terms of cumulated rainfalls with the occurrence of landslides for monthly rainfall amounts higher than 200 mm during one of the winter months. The average cumulated rainfall for the three months are very variable for the various periods and amount to 166 ± 60 mm (1956–1974), 184 ± 105 mm (1974–1982), 132 ± 64 mm (1982–1995), 133 ± 62 mm (1995–2000), 92 ± 81 mm (2000–2004) and 99 ± 32 mm (2004–2009). High amounts of rainfall (including snow) are identified for the period 1974–1982 which is affected by the occurrence of many landslide (re)-activations.

Other triggering factors play a role in slope destabilization, such as snow coverage (rapid melting; Cardinali et al., 2000), rapid pore water pressure changes (Maquaire et al., 2003), and high magnitude earthquakes or, as in the French Alps multiple low-magnitude earthquakes (Sanchez et al., 2010). In the Ubaye valley, numerous M_w 2.0 to 4.0 earthquakes were recorded during the periods 2003–2004 and 2012–2015 (Leclère et al., 2013). For instance, the strongest and shallowest earthquakes have significant effect on active landslides (e.g. daily displacement monitored by permanent GNSS stations installed at the upper part of the La Valette landslide were multiplied by a factor of 5 in the days following a 10 km deep, 4.8 earthquake on 7 April 2014). The catalogues of earthquakes of M_w above 2.5, observed within a radius of 30 km around the city of Barcelonnette, are plotted against the previously described datasets (Fig. 15d). In 1977, nine earthquakes were recorded, corresponding also to a period of high rainfall amounts, and many landslide (re)-activations were observed. For the period 1981–1985, numerous seismic events were recorded; this period corresponds also to a higher number of landslide events.

NHESSD
3, 2051–2098, 2015

5 Conclusion

The interpretation of a series of aerial photographs allows us to increase the number of detected landslide events (new landslide or landslide reactivation) than those already present in former historical landslide catalogue, and to create a multi-date inventory. However, the interpretation remains difficult and clearly depends on (1) the skills of the geoscientist, and (2) the knowledge of the field conditions in order to properly recognize landslide features. L-band D-InSAR allowed the detection of slow-moving landslides on a portion of the territory (around 60 %) according to the SAR properties. It provided additional information on the active landslides (sometimes unknown or under forest) for the recent time.

Some indicators have been used for the evaluation of landslide intensity. Differences in frequency-area distributions are observed according to the geomorphological settings of the landslides and their degree of activity. It also reveals the difficulty to map the small size events (i.e. $< 540\,m^2$).

As multi-temporal inventories are time-consuming to prepare, only few works have been published on the temporal probability of reactivation (Coe et al., 2000; Guzzetti et al., 2005; Lopez-Saez et al., 2012). The approach presented in this paper allows determination of quantitative probabilities of reactivation estimated directly from the frequency of past landslide events. The approach uses a Poisson probability model based on some assumptions even if most hazardous events, and especially landslides, are probably not independent and do not occur randomly (Coe et al., 2000). Indeed, a landslide reactivation can increase or decrease the slope susceptibility to future landslides, thus creating a low-to-high instability in the future. Changes in land use or climatic conditions also affect the future occurrence of landslides.

The comparison of landslide activity measured by the multi-date inventory and by the landslide historical catalogue pointed out the incompleteness of the historical catalogue. The multi-date inventory correlated to the meteorological events and the historical landslide events catalogue shows that it is more complete in some cases and

NHESSD
3, 2051–2098, 2015

provides useful additional information. However, it only allows an expert to determine periods of activity and not precise years or even months. In addition, this technique induces underestimation of small events, mainly due to the limitations in the visual analysis because of the sources data and the terrain conditions.

Even if they are definitively more complicated to interpret, construction of large multi-source datasets is mandatory for the analysis of landslide occurrences. Preliminary statistical analyses of landslide inventories are relevant to explore the spatial and temporal distribution of landslides events.

Acknowledgements. This work has been supported by the Marie Curie Research and Initial Training Network *"CHANGES: Changing Hydro-meteorological Risks as Analyzed by a New Generation of European Scientists"*, funded by the European Community's 7th Framework Programme FP7/2007–2013 under Grant Agreement No. 263953. The orthophotographs and elevation data were provided by IGN (*Institut Géographique National*) and other public partners. The access to ALOS/PALSAR images was given by the Japan Aerospace eXploration Agency (JAXA) and the European Space Agency (ESA) under the contract C1P.8859. The historical catalogue of landslide events was provided by the RTM-04 (*Restauration des Terrains en Montagne*) service of *Département des Alpes-de-Haute-Provence*. The authors would like to thank M. Rossi and M. Santangelo (CNR-Irpi, Italy) for their advices.

References

Barlow, J., Franklin, S., and Martin, Y.: High spatial resolution satellite imagery, DEM derivatives, and image segmentation for the detection of mass wasting processes, Photogramm. Eng. Rem. S., 72, 687–692, 2006.

Campbell, R. H.: Isopleth map of landslide deposits, Point Dume quadrangle, Los Angeles County, California, an experiment in generalizing and quantifying areal distribution of landslides, US Geological Survey Miscellaneous Field Studies Map MF-535, scale 1 : 24 000, 1973.

Canuti, P., Casagli, N., Ermini, L., Fanti, R., and Farina, P.: Landslide activity as a geoindicator in Italy: significance and new perspectives from remote sensing, Environ. Geol., 45, 907–919, 2004.

NHESSD

3, 2051–2098, 2015

Cara, M., Cansi, Y., Schlupp, A., and the SI-Hex Working Group: SI-Hex: a new catalogue of instrumental seismicity in metropolitan France, B. Soc. Geol. Fr., 186, 3–19, 2014.
Cardinali, M., Ardizzone, F., Galli, M., Guzzetti, F., and Reichenbach, P.: Landslides triggered by rapid snow melting: the December 1996–January 1997 event in Central Italy, in: Proceedings 1st Plinius Conference, Maratea, 439–448, 2000.
Cascini, L., Fornaro, G., and Peduto, D.: Analysis at medium scale of low-resolution DInSAR data in slow-moving landslide-affected areas, ISPRS J. Photogramm., 64, 598–611, 2009.
Coe, J. A., Michael, J. A., Crovelli, R. A., and Savage, W. Z.: Preliminary map showing landslide densities, mean recurrence intervals, and exceedance probabilities as determined from historic records, Seattle, Washington, USGS Open-File Report 00-0303, 2000.
Colesanti, C. and Wasowski, J.: Investigating landslides with space-borne Synthetic Aperture Radar (SAR) interferometry, Eng. Geol., 88, 173–199, 2006.
Corominas, J.: The angle of reach as a mobility index for small and large landslides, Can. Geotech. J., 33, 260–271, 1996.
Corominas, J., van Westen, C. J., Frattini, P., Cascini, L., Malet, J.-P., Fotopoulou, S., Catani, F., van den Eeckhaut, M., Mavrouli, O.-C., Agliardi, F., Pitilakis, K., Winter, M. G., Pastor, M., Ferlisi, S., Tofani, V., Hervás, J., and Smith, J. T.: Recommendations for the quantitative assessment of landslide risk, B. Eng. Geol. Environ., 73, 209–263, 2014.
Crovelli, R. A.: Probability models for estimation of number and costs of landslides, US Geological Survey Open File Report 00-249, 2000.
Cruden, D. and Varnes, D.: Landslide types and processes, in: Landslides: Investigation and Mitigation, edited by: Turner, R. L. and Schuster, A. K., Washington, D.C., 36–75, 1996.
DeGraff, J. V. and Canuti, P.: Using isopleth mapping to evaluate landslide activity in relation to agricultural practices, Bull. Int. Assoc. Eng. Geol., 38, 61–71, 1988.
Doin, M.-P., Lodge, F., Guillaso, S., Jolivet, R., Lasserre, C., Ducret, G., Grandin, R., Pathier, E., and Pinel, V.: Presentation of the small baseline processing chain on a case example: the Etna deformation monitoring from 2003 to 2010 using ENVISAT data, in: Proc. "Fringe 2011 Workshop", Frascati, Italy, 19–23 September 2011, 303–204, 2011.
Fiorucci, F., Cardinali, M., Carlà, R., Rossi, M., Mondini, A. C., Santurri, L., Ardizzone, F., and Guzzetti, F.: Seasonal landslide mapping and estimation of landslide mobilization rates using aerial and satellite images, Geomorphology, 129, 59–70, 2011.

NHESSD
3, 2051–2098, 2015

Flageollet, J.-C., Maquaire, O., Martin, B., and Weber, D.: Landslides and climatic conditions in the Barcelonnette and Vars basins (Southern French Alps, France), Geomorphology, 30, 65–78, 1999.
Florsheim, J. and Nichols, A.: Landslide area probability density function statistics to assess historical landslide magnitude and frequency in coastal California, Catena, 109, 129–138, 2013.
Günther, A., Reichenbach, P., Malet, J.-P., van den Eeckhaut, M., Hervás, J., Dashwood, C., and Guzzetti, F.: Tier-based approaches for landslide susceptibility assessment over Europe, Landslides, 10, 529–546, 2013.
Guzzetti, F., Malamud, B. D., Turcotte, D. L., and Reichenbach, P.: Power-law correlations of landslide areas in central Italy, Earth Planet. Sc. Lett., 195, 169–183, 2002.
Guzzetti, F., Reichenbach, P., and Wieczorek, G. F.: Rockfall hazard and risk assessment in the Yosemite Valley, California, USA, Nat. Hazards Earth Syst. Sci., 3, 491–503, doi:10.5194/nhess-3-491-2003, 2003.
Guzzetti, F., Reichenbach, P., Cardinali, M., Galli, M., and Ardizzone, F.: Probabilistic landslide hazard assessment at the basin scale, Geomorphology, 72, 272–299, 2005.
Guzzetti, F., Mondini, A. C., Cardinali, M., Fiorucci, F., Santangelo, M., and Chang, K.-T.: Landslide inventory maps: new tools for an old problem, Earth-Sci. Rev., 112, 42–66, 2012.
Hanssen, R. F.: Radar interferometry: data interpretation and error analysis, Springer, 2001.
Jaiswal, P., van Westen, C. J., and Jetten, V.: Quantitative assessment of landslide hazard along transportation lines using historical records, Landslides, 8, 279–291, 2011.
Jorda, M.: Morphogenèse et évolution des paysages des Alpes de Haute-Provence depuis le Tardiglaciaire. Facteurs naturels et facteurs anthropiques, Bull. l'Association des Géographes Français, 472, 295–304, 1980.
Kurtz, C., Stumpf, A., Malet, J.-P., Gançarski, P., Puissant, A., and Passat, N.: Hierarchical extraction of landslides from multiresolution remotely sensed optical images, ISPRS J. Photogramm., 87, 122–136, 2014.
Leclère, H., Daniel, G., Fabbri, O., Cappa, F., and Thouvenot, F.: Tracking fluid pressure buildup from focal mechanisms during the 2003–2004 Ubaye seismic swarm, France, J. Geophys. Res., 118, 4461–4476, 2013.
Lopez-Saez, J., Corona, C., Stöffel, M., Astrade, L., Berger, F., and Malet, J.-P.: Dendrogeomorphic reconstruction of past landslide reactivation with seasonal precision: the Bois Noir landslide, southeast French Alps, Landslides, 9, 189–203, 2011.

NHESSD
3, 2051–2098, 2015

Lopez-Saez, J., Corona, C., Stöffel, M., Schoeneich, P., and Berger, F.: Probability maps of landslide reactivation derived from tree-ring records: Pra Bellon landslide, southern French Alps, Geomorphology, 138, 189–202, 2012.
Lopez-Saez, J., Corona, C., Stöffel, M., and Berger, F.: High-resolution fingerprints of past landsliding and spatially explicit, probabilistic assessment of future reactivations: Aiguettes landslide, Southeastern French Alps, Tectonophysics, 602, 355–369, 2013.
Lu, P., Casagli, N., Catani, F., and Tofani, V.: Persistent Scatterers Interferometry Hotspot and Cluster Analysis (PSI-HCA) for detection of extremely slow-moving landslides, Int. J. Remote Sens., 33, 466–489, 2012.
Malamud, B. D., Turcotte, D. L., Guzzetti, F., and Reichenbach, P.: Landslide inventories and their statistical properties, Earth Surf. Proc. Land., 29, 687–711, 2004.
Malet, J.-P.: Les "glissements de type écoulement" dans les marnes noires des Alpes du Sud. Morphologie, fonctionnement et modélisation hydro-mécanique, Ph.D. thesis, University Louis Pasteur, Strasbourg, 364, 2003.
Malet, J.-P., Laigle, D., Remaître, A., and Maquaire, O.: Triggering conditions and mobility of debris flows associated to complex earthflows, Geomorphology, 66, 215–235, 2005a.
Malet, J.-P., van Asch, Th. W. J., van Beek, R., and Maquaire, O.: Forecasting the behaviour of complex landslides with a spatially distributed hydrological model, Nat. Hazards Earth Syst. Sci., 5, 71–85, doi:10.5194/nhess-5-71-2005, 2005b.
Maquaire, O., Malet, J.-P., Remaître, A., Locat, J., Klotz, S., and Guillon, J.: Instability conditions of marly hillslopes: towards landsliding or gullying?, The case of the Barcelonnette Basin, South East France, Eng. Geol., 70, 109–130, 2003.
Massonnet, D. and Feigl, K. L.: Radar Interferometry and its application to changes in the Earth's surface, Rev. Geophys., 36, 441–500, 1998.
McCalpin, J.: Preliminary age classification of landslides for inventory mapping, 99–111, 1984.
Metternicht, G., Hurni, L., and Gogu, R.: Remote sensing of landslides: an analysis of the potential contribution to geo-spatial systems for hazard assessment in mountainous environments, Remote Sens. Environ., 98, 284–303, 2005.
Mondini, A. C., Chang, K.-T., and Yin, H.-Y.: Combining multiple change detection indices for mapping landslides triggered by typhoons, Geomorphology, 134, 440–451, 2011.
Razak, K. A., Straatsma, M. W., van Westen, C. J., Malet, J.-P., and de Jong, S. M.: Airborne laser scanning of forested landslides characterization: terrain model quality and visualization, Geomorphology, 126, 186–200, 2011.

NHESSD
3, 2051–2098, 2015

Remaître, A. and Malet, J.-P.: Rainfall patterns for landslides and debris flows at various time scales for the Southeastern French Alps. Landslides, submitted, 2015.
Remaître, A., Malet, J., Maquaire, O., Ancey, C., and Locat, J.: Flow behaviour and runout modelling of a complex debris flow in a clay-shale basin, Earth-Sci. Rev., 30, 479–488, 2005.
Rosen, P. A., Hensley, S., Joughin, I., Li, F., Madsen, S. N., Rodríguez, E., and Goldstein, R. M.: Synthetic Aperture Radar interferometry, P. IEEE, 88, 333–382, 2000.
Rosen, P. A., Hensley, S., Peltzer, G., and Simons, M.: Updated repeat orbit interferometry package released, EOS T. Am. Geophys. Un., 85, 47–47, 2004.
Rossi, M., Ardizzone, F., Cardinali, M., Fiorucci, F., Marchesini, I., Mondini, A. C., Santangelo, M., Ghosh, S., Riguer, D. E. L., Lahousse, T., Chang, K. T., and Guzzetti, F.: A tool for the estimation of the distribution of landslide area in R, Geophys. Res. Abstr., 14, EGU2012–9438–1, 2012.
Salomé, A. I. and Beukenkamp, P.: Geomorphologogical mapping of a high-mountain area in black and white, Z. Geomorphol., 33, 19–23, 1989.
Sanchez, G., Rolland, Y., Corsini, M., Braucher, R., Bourlès, D., Arnold, M., and Aumaître, G., Relationships between tectonics, slope instability and climate change: cosmic ray exposure dating of active faults, landslides and glacial surfaces in the SW Alps, Geomorphology, 117, 1–13, 2010.
Schlögel, R., Torgoev, I., De Marneffe, C., and Havenith, H.-B.: Evidence of a changing size-frequency distribution of landslides in the Kyrgyz Tien Shan, Central Asia, Earth Surf. Proc. Land., 36, 1658–1669, 2011.
Schlögel, R., Doubre, C., Malet, J.-P., and Masson, F.: Landslide deformation monitoring with ALOS/PALSAR imagery: a D-InSAR geormorphological interpretation method, Geomorphology, 231, 314–330, 2015.
Singhroy, V. and Molch, K.: Characterizing and monitoring rockslides from SAR techniques, Adv. Space Res., 33, 290–295, 2004.
Soriso Valvo, M.: Landslides: from inventory to risk, in: Proc. of the 1st European conference on landslides, Prague, Czech Republic, 24–26 June 2002, Balkema, Rotterdam, 59–79, 2002.
Stark, C. P. and Hovius, N.: The characterization of landslide size distributions, Geophys. Res. Lett., 28, 1091–1094, 2001.
Stien, D.: Glissements de terrains et enjeux dans la vallée de l'Ubaye et le pays de Seyne, Rapport ONF-RTM, Division de Barcelonnette, France, 2001.

NHESSD
3, 2051–2098, 2015

Thiery, Y.: Susceptibilité du Bassin de Barcelonnette (Alpes du sud, France) aux "mouvements de versant"?: cartographie morphodynamique, analyse spatiale et modélisation probabiliste, Ph.D. thesis, Université de Caen-Basse-Normandie, 2007.
Thiery, Y., Malet, J.-P., Sterlacchini, S., Puissant, A., and Maquaire, O.: Landslide susceptibility assessment by bivariate methods at large scales: application to a complex mountainous environment, Geomorphology, 92, 38–59, 2007.
Thiery, Y., Maquaire, O., and Fressard, M.: Application of expert rules in indirect approaches for landslide susceptibility assessment, Landslides, 11, 411–424, 2014.
Travelletti, J., Malet, J.-P., and Delacourt, C.: Image-based correlation of laser scanning point cloud time series for landslide monitoring, Int. J. Appl. Earth Obs., 32, 1–18, 2014.
van den Eeckhaut, M., Poesen, J., Verstraeten, G., Vanacker, V., Moeyersons, J., Nyssen, J., and van Beek, L. P. H.: The effectiveness of hillshade maps and expert knowledge in mapping old deep-seated landslides, Geomorphology, 67, 351–363, 2005.
van den Eeckhaut, M., Poesen, J., Govers, G., Verstraeten, G., and Demoulin, A.: Characteristics of the size distribution of recent and historical landslides in a populated hilly region, Earth Planet. Sc. Lett., 256, 588–603, 2007.
Varnes, D. J.: Slope movement types and processes, in: Special Report 176: Landslides: Analysis and Control, edited by: Schuster, R. L. and Krizek, R. J., Transportation and Road Research Board, National Academy of Science, Washington, D.C., 11–33, 1978.
Wills, C. J. and McCrink, T. P.: Comparing landslide inventories: the map depends on the method, Environ. Eng. Geosci., 8, 279–293, 2002.
Wright, R. H., Campbell, R. H., and Nilsen, T. H.: Preparation and use of isopleth maps of landslide deposits, Geology, 2, 483–486, 1974.
ZERMOS: Carte des Zones Exposées à des Risques liés aux Mouvements du Sol et du sous-sol, Barcelonnette, 1/25 000, Bureau de Recherches Géologiques et Minières, 1975.
Zhao, C., Lu, Z., Zhang, Q., and de la Fuente, J.: Large-area landslide detection and monitoring with ALOS/PALSAR imagery data over Northern California and Southern Oregon, USA, Remote Sens. Environ., 124, 348–359, 2012.

NHESSD
3, 2051–2098, 2015

Table 1. Dataset used for landslide recognition and mapping.

	Type of data	Source	Resolution	Scale	Date	Landslide information
1.	Orthophotograph	IGN	1.5 m	1 : 35 000	31 Jul 1956	Location/Type
2.	Orthophotograph	IGN	1.0 m	1 : 15 000	10 Jul 1974	Location/Type
3.	Orthophotograph	IGN	1.0 m	1 : 20 000	1 Jul 1982	Location/Type
4.	Orthophotograph	IGN	0.7 m	1 : 25 000	25 Jul 1995	Location/Type
5.	Orthophotograph	IGN	0.5 m	1 : 25 000	24 Jun 2000	Location/Type
6.	Orthophotograph	IGN	0.5 m	1 : 25 000	3 Jul 2004	Location/Type
7.	Orthophotograph	IGN	0.5 m	1 : 25 000	19 Jul 2009	Location/Type
8.	Airborne SAR DSM	IfSAR-Fugro	5.0 m	–	2009	Location/Type
9.	Elevation-line DSM	EOST[1]	10 m	–	2004	Location/Type
10.	DSM – BD-ALTI	IGN	25 m	–	–	Location
11.	Geological map	BRGM	–	1 : 25 000	1974	Location
12.	Geomorphological map	ZERMOS	–	1 : 25 000	1975	Location
13.	Geomorphological map	Utrecht Univ.[2]	–	1 : 25 000	1989	Location
14.	Geomorphological map	RTM[3]	–	1 : 10 000	2001	Location
15.	Dendrogeomorphic data	Irstea[4]	–	1 : 3000	1850–2004	Location/Time
16.	L-band SAR images	EOST[5]	10 m	–	2007–2010	Location/Time/Intensity
17.	Geomorphological inventory	EOST[1]	–	1 : 5000	2004	Location/Time/Intensity
18.	Historical catalogue	RTM/BRGM	–	–	1850–2012	Location/Time
19.	Historical reports	RTM[3]	–	–	1990–2012	Location/Time

[1] Thiery (2007); [2] Salomé & Beukenkamp (1989); [3] Stien (2001); [4] Lopez-Saez et al. (2012; 2013); [5] Schlögel et al. (2015)

NHESSD
3, 2051–2098, 2015

Table 2. Landslide attributes integrated in the database.

Attributes	Definition	Descriptors/Units
Type (and sub-type)	Typology of Cruden and Varnes (1996)	Deep-seated rotational slide, deep-seated translational slide, shallow translational slide, complex mudslide
Degree of activity	Definition adapted after McCalpin (1984) and Varnes (1978)	relict, dormant, active
Size	Area/perimeter	m^2
Elevation range	Difference between the highest and the lowest elevation points measured along the slide perimeter	m
Longest distance (runout)	Horizontal distance between the highest and lowest points located along the slide perimeter	m
Angle of reach	Angle of the line joining the scarp and the landslide toe	°
Vegetation index	Qualitative estimation of the degree of activity	0 (reactivation) 1 (no change)
Uncertainty index	Estimation of quality and reliability of the visual interpretation	1 (reliable) 2 (supposed)

NHESSD
3, 2051–2098, 2015

Table 3. Descriptive statistics of the geomorphological inventories for the different landslide types and degrees of activity. The geomorphological inventories are divided into groups according to the degree of activity: *R* (relict, i.e. inactive landslides), *D* (dormant, i.e. inactive-mature landslides), G_{56} (active landslide in 1956) and G_{09} (active landslides in 2009). The landslide types are deep-seated rotational, deep-seated translational, shallow translational and mudslide.

	Date	Type	Activity	Number	Area (km^2)	Density
R	Very old	Deep-seated rot./transl.	Relict	59	16.7	7.1 %
D	Old	Deep-seated rot./transl.	Dormant	115	11.5	4.9 %
G_{56}	< 1956	all	Active	512	13.7	5.8 %
		Deep-seated rotational	Active	174	9.3	3.9 %
		Deep-seated translational	Active	287	4.1	1.7 %
		Shallow translational	Active	46	0.2	0.1 %
		Mudslide	Active	5	0.2	0.1 %
G_{09}	< 2009	all	Active	614	16.6	7.1 %
		Deep-seated rotational	Active	208	10.7	4.5 %
		Deep-seated translational	Active	345	4.9	2.1 %
		Shallow translational	Active	55	0.4	0.2 %
		Mudslide	Active	6	0.7	0.3 %

NHESSD
3, 2051–2098, 2015

Table 4. Number and size of landslides for different time periods: A_1 (before 1956), A_2 (from 1956 to 1974), A_3 (from 1974 to 1982), A_4 (from 1982 to 1995), A_5 (from 1995 to 2000), A_6 (from 2000 to 2004) and A_7 (from 2004 to 2009).

	Date	Activity	Number	Number yr^{-1}	Area yr^{-1}	Density
A_1	* < 1956	Activated	74	2.6	5.9×10^4	0.5
A_2	> 1956 to < 1974	Reactivated	131	7.3	1.8×10^5	1.4
		New	28	1.6	1.9×10^4	0.1
A_3	> 1974 to < 1982	Reactivated	265	33.1	7.9×10^5	2.7
		New	35	4.4	2.0×10^4	0.1
A_4	> 1982 to < 1995	Reactivated	148	11.4	4.3×10^5	2.4
		New	13	1.0	4.8×10^3	0.1
A_5	> 1995 to < 2000	Reactivated	103	20.6	8.0×10^5	1.7
		New	13	2.6	4.3×10^4	0.1
A_6	> 2000 to < 2004	Reactivated	111	27.8	9.4×10^5	1.6
		New	4	1.0	8.3×10^3	0.1
A_7	> 2004 to < 2009	Reactivated	116	23.2	1.4×10^6	3.0
		New	11	2.2	1.6×10^5	0.3

* the precise date is unknown.

NHESSD
3, 2051–2098, 2015

Table 5. Temporal probability of landslide reactivation for 4 return periods. The temporal probabilities are expressed in landslide area and relative percentage of landslide areas (see Fig. 12). The temporal probability is the probability of landslide reactivation for the active landslides observed in the study area (Fig. 5a) and is calculated with a Poisson probability model.

$P(N \geq 1)$	]0–0.2			]0.2–0.4			]0.4–0.6			]0.6–0.8			]0.8–1.0		
years	# cells	area (km^2)	%	# cells	area (km^2)	%	# cells	area (km^2)	%	# cells	area (km^2)	%	# cells	area (km^2)	%
5	540	33.8	65.7	261	16.3	31.8	21	1.3	2.6	0	0	0	0	0	0
10	334	20.9	40.6	206	12.9	25.1	235	14.7	28.6	47	2.9	5.7	0	0	0
25	0	0	0	334	20.9	40.6	0	0	0	337	21.1	41.0	151	9.4	8.4
50	0	0	0	0	0	0	0	0	0	334	20.9	40.6	488	30.5	9.4

NHESSD
3, 2051–2098, 2015

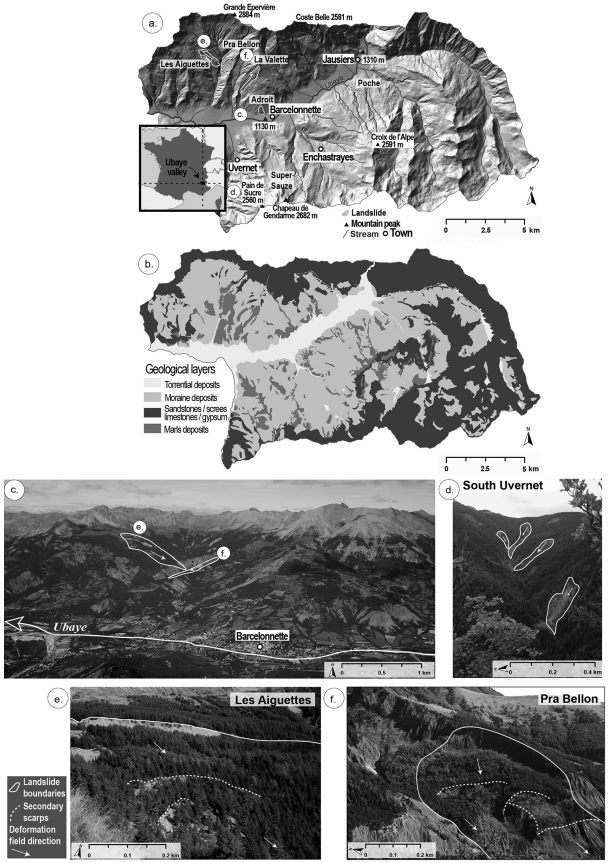

Figure 1. Location of the study area and examples of landslide types. **(a)** Topography of the area and location of the monitored landslides. **(b)** Simplified geological map. **(c)** Typical landscape of the south-facing slope located on the right riverbank of the Ubaye River. **(d)** Shallow translational landslides located south of Uvernet in Riou Chanal catchment. **(e)** Deep-seated translational landslide of Les Aiguettes. **(f)** Deep-seated rotational landslide of Pra-Bellon.

NHESSD
3, 2051–2098, 2015

Analysis of a landslide multi-date inventory in a complex mountain landscape

R. Schlögel et al.

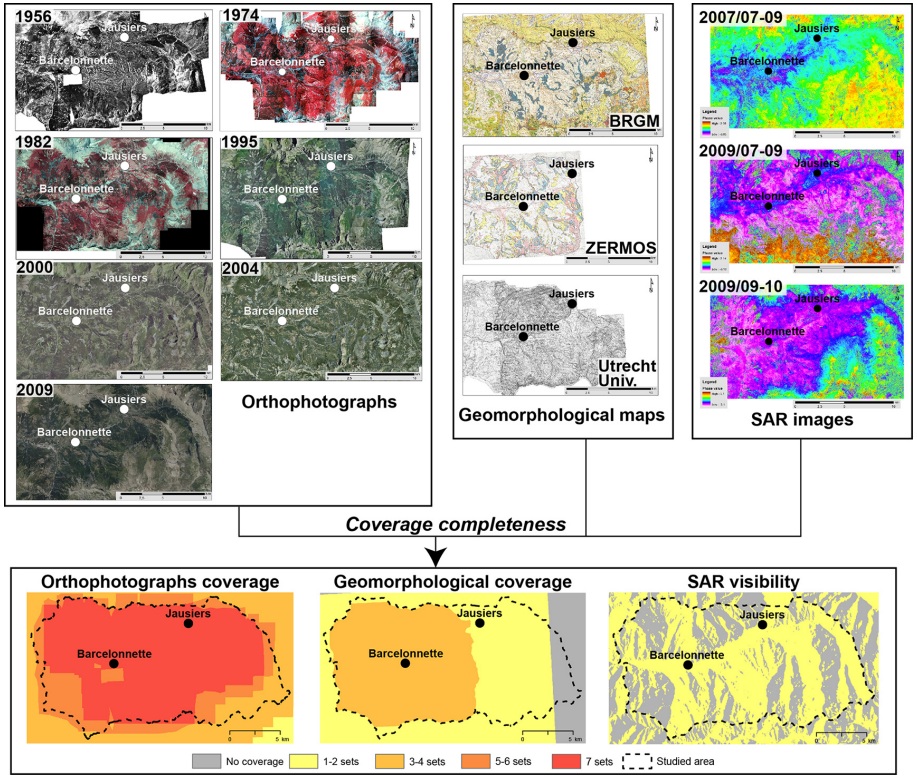

Figure 2. Documents used for landslide recognition and mapping. The figure indicates the completeness of the spatial coverage for each document type (orthophotographs, geomorphological maps, SAR images).

NHESSD
3, 2051–2098, 2015

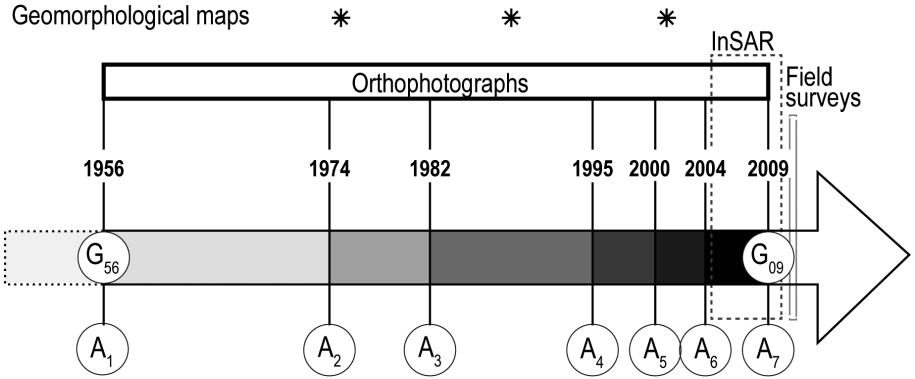

Figure 3. Acquisition dates of the documents and name of the different geomorphological inventories for the various periods of analysis. The detailed geomorphological inventories G_{56} and G_{09} are for the years 1956 and 2009; the geomorphological inventories A_n are inventories with the landslides recorded for the periods < 1956 (A_1), 1956–1974 (A_2), 1974–1982 (A_3), 1982–1995 (A_4), 1995–2000 (A_5), 2000–2004 (A_6) and 2004–2009 (A_7).

NHESSD
3, 2051–2098, 2015

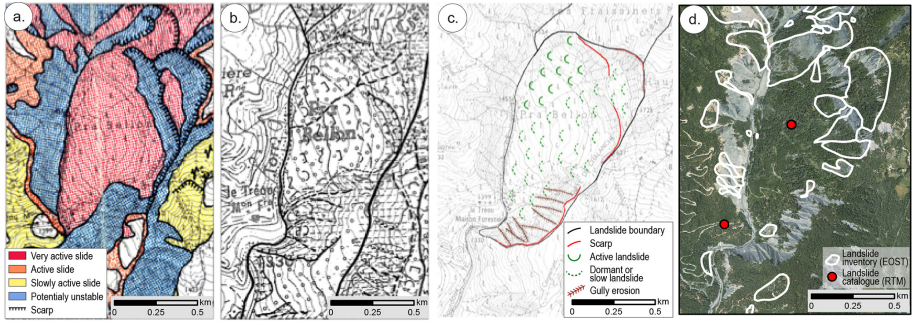

Figure 4. Methodology used for combining the information from several geomorphological maps with the example of the Pra-Bellon landslide. **(a)** Geomorphological map from 1975 (ZERMOS, 1975). **(b)** Geomorphological map from 1989 (Utrecht University; Salomé and Beukenkamp, 1989). **(c)** Geomorphological map from 2001 (Stien, 2001). **(d)** Landslide geomorphological inventory map from 2007 (Thiery, 2007).

NHESSD
3, 2051–2098, 2015

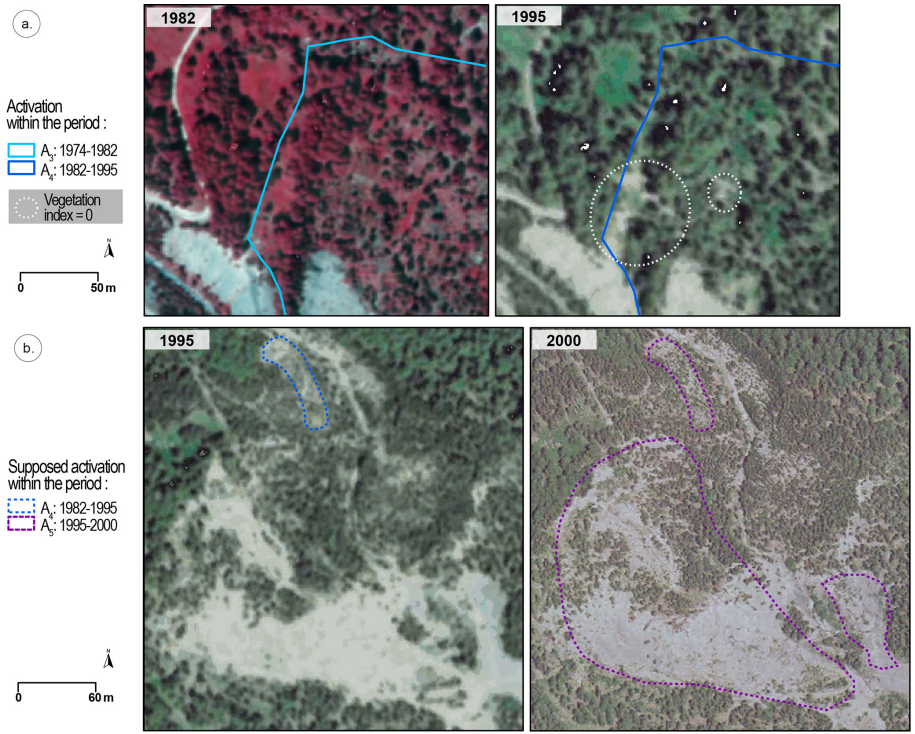

Figure 5. Example of landslide reactivation and categorization of the vegetation and uncertainty index. **(a)** Example of a certain landslide reactivation corresponding to a vegetation index of 0 and an uncertainty index of 1. **(b)** Example of a supposed reactivation corresponding to a vegetation index of 0 and an uncertainty index of 2.

NHESSD
3, 2051–2098, 2015

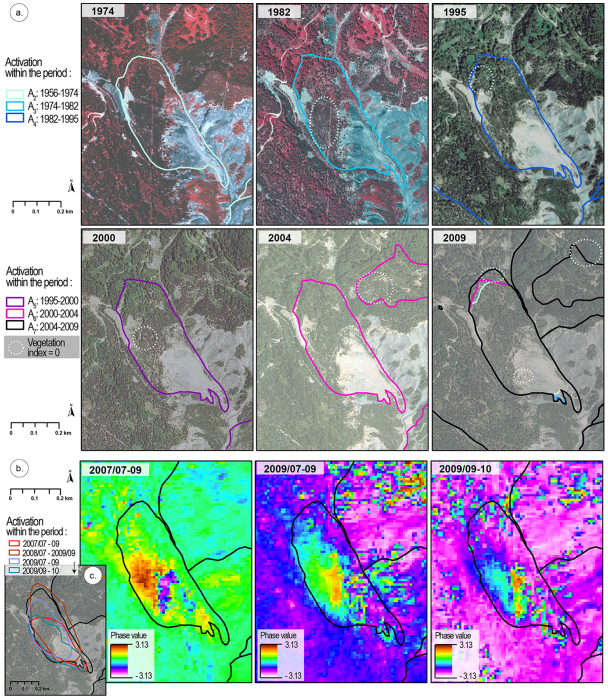

Figure 6. Combination of orthophotographs and SAR interferograms for the creation of the landslide geomorphological inventories. **(a)** Extension of active landslides in 1974, 1982, 1995, 2000, 2004, 2009 on the orthophotograph on a slope located in the Riou-Bourdoux catchment. **(b)** SAR interferograms of the same slope with several landslide signals corresponding to specific spatial arrangement of phase values for three periods of 46 days (July–September 2007, July–September 2009, September–October 2009). The extension of the landslides interpreted by visual interpretation of the series of orthophotographs and from field recognitions is indicated with the black line. Sub-units within the landslides of various surface displacement rates are identified. **(c)** Interpreted extension of the landslide sub-units from the SAR interferograms for three time periods of 46 days.

NHESSD
3, 2051–2098, 2015

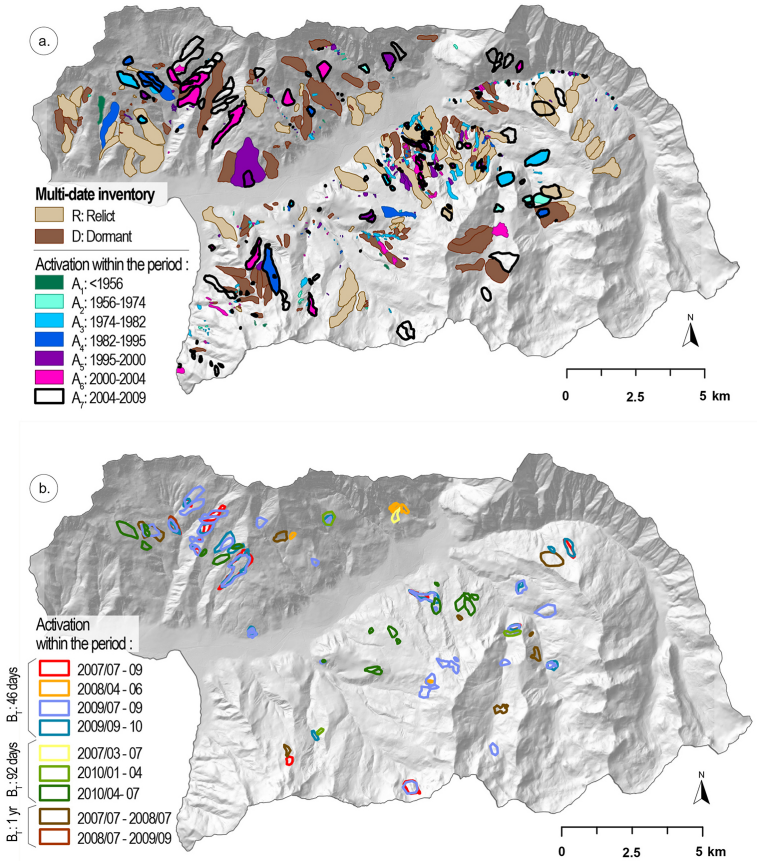

Figure 7. Multi-date landslide geomorphological inventory maps. **(a)** Map indicating the landslide for different degree of activity (R: relict; D: dormant; A_1–A_7: active) for the periods A_1 (< 1956) A_2 (1956–1974), A_3 (1974–1982), A_4 (1982–1995), A_5 (1995–2000) A_6 (2000–2004) and A_7 (2004–2009). **(b)** Map of landslide activation for the period 2007–2010 detected by InSAR with different temporal baselines (B_T) of 46, 92 days and 1 year.

NHESSD
3, 2051–2098, 2015

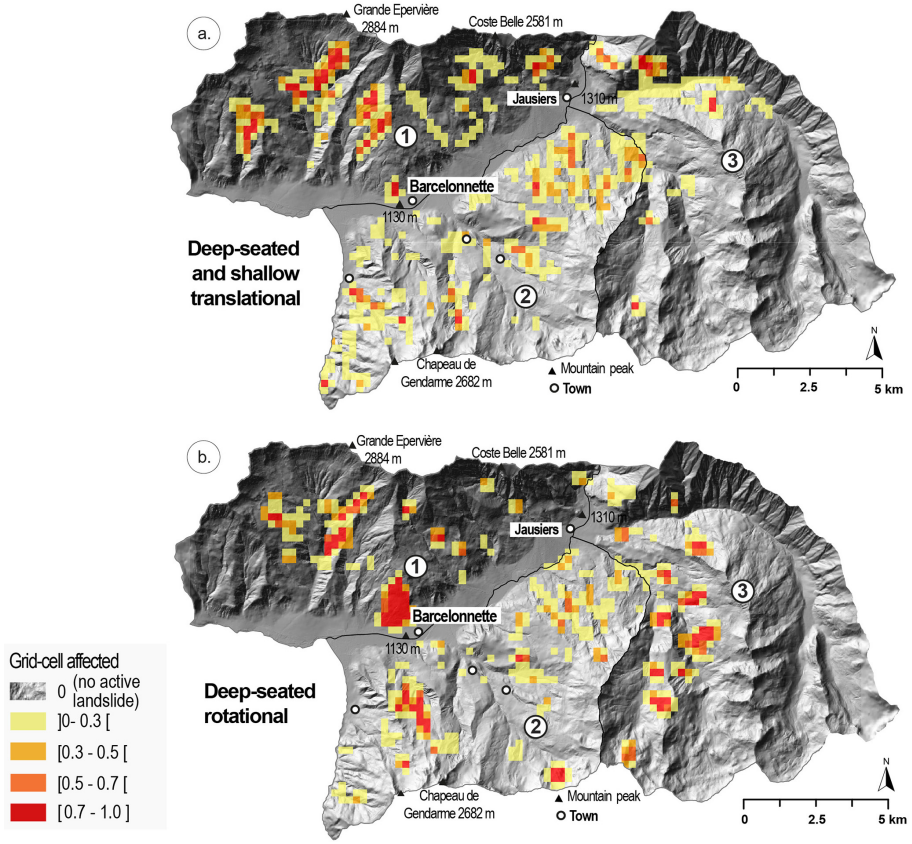

Figure 8. Landslide density maps. **(a)** Percentage of grid-cell affected by active deep-seated and shallow translational slides. **(b)** Percentage of grid-cell affected by active deep-seated rotational slides. The grid-cell dimension is 250 m.

NHESSD
3, 2051–2098, 2015

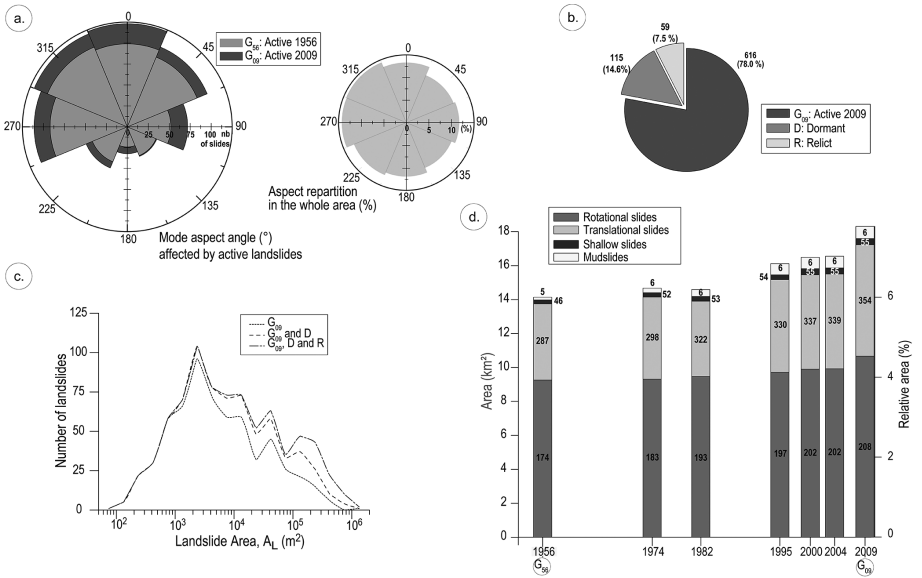

Figure 9. Statistics of the landslides observed in the Ubaye valley according to **(a)** the distribution of slope aspects; **(b)** the landslide degree of activity (relict, dormant and active), **(c)** the landslide distribution in terms of number and area, and **(d)** the evolution of area affected by different landslide types from 1956 to 2009. The number of landslide per type is indicated on the graph.

NHESSD
3, 2051–2098, 2015

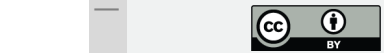

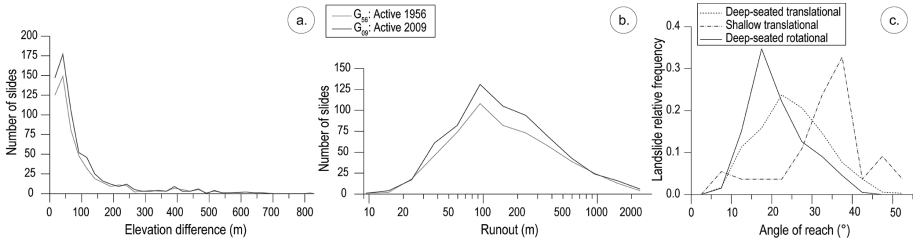

Figure 10. Analysis of the landslide geomorphological parameters: **(a)** Elevation difference of the landslides observed in 1956 and 2009. **(b)** Runout distance of the landslides observed in 1956 and 2009. **(c)** Angle of reach for the different landslide types in 2009.

NHESSD
3, 2051–2098, 2015

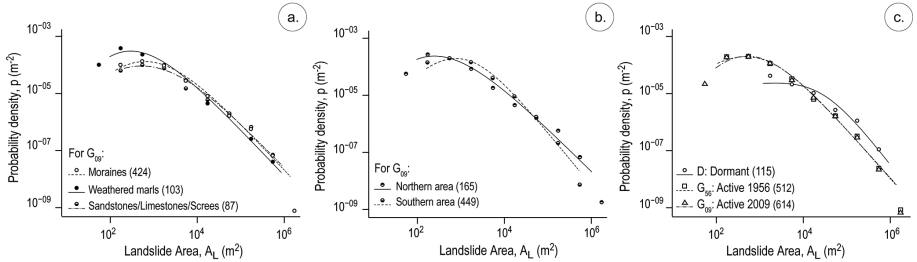

Figure 11. Landslide frequency-area distributions and maximum-likelihood fit of a Double-Pareto Simplified model. **(a)** Frequency-areas distributions for three categories of lithology of the landslide source area; **(b)** Frequency-areas distributions for two morphological units of the Ubaye valley (right and left riverbanks of the Ubaye River corresponding, respectively, to the northern and southern areas). **(c)** Frequency-areas distributions for three categories of degree of activity.

NHESSD
3, 2051–2098, 2015

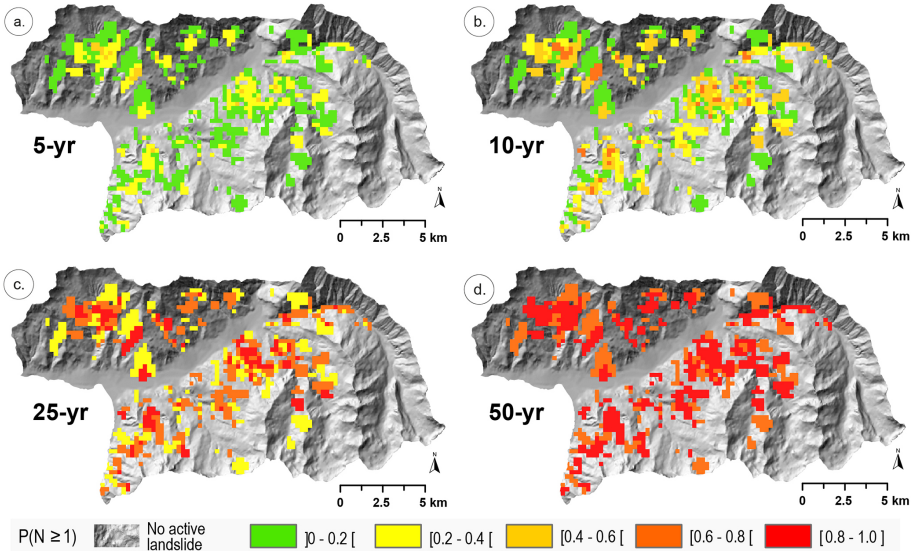

Figure 12. Exceedance probability of temporal occurrence of landslide reactivation calculated from the mean recurrence interval of past landslides (Fig. 5a) with a Poisson probability model. Exceedance probability is calculated for four return periods (5, 10, 25 and 50 years). A probability of zero is obtained in the areas where no active landslides are observed.

NHESSD
3, 2051–2098, 2015

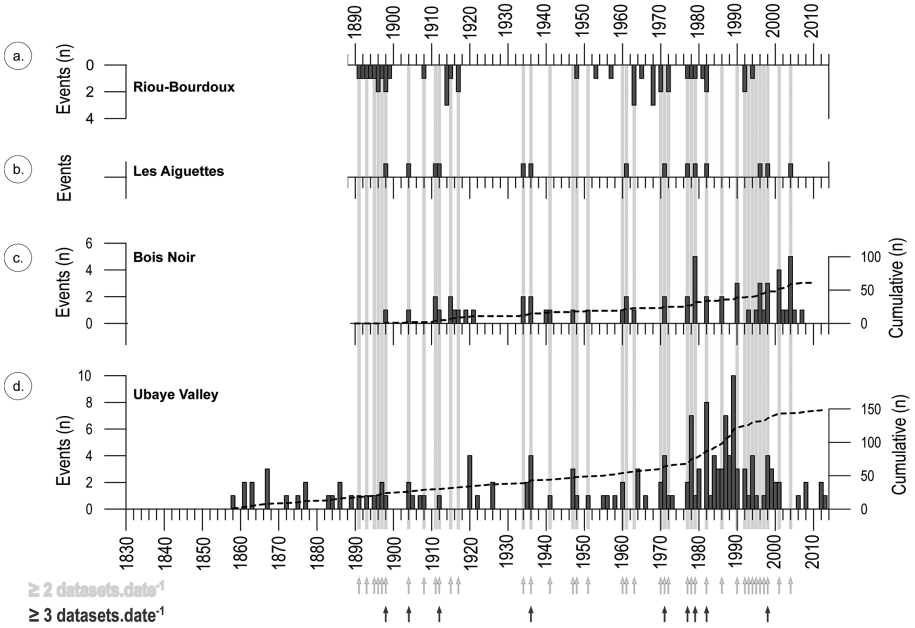

Figure 13. Comparative analysis of periods of landslide activity recorded in several datasets. **(a)** Landslide dendrogeomorphological observations for the Riou-Bourdoux catchment (Lopez-Saez et al., 2013); **(b)** Dendrogeomorphic observations for the Pra-Bellon landslide (Lopez-Saez et al., 2012); **(c)** Dendrogeomorphic observations for the Les Aiguettes landslide (Lopez-Saez et al., 2011) and **(d)** RTM and BRGM landslide catalogues for the Ubaye valley.

NHESSD
3, 2051–2098, 2015

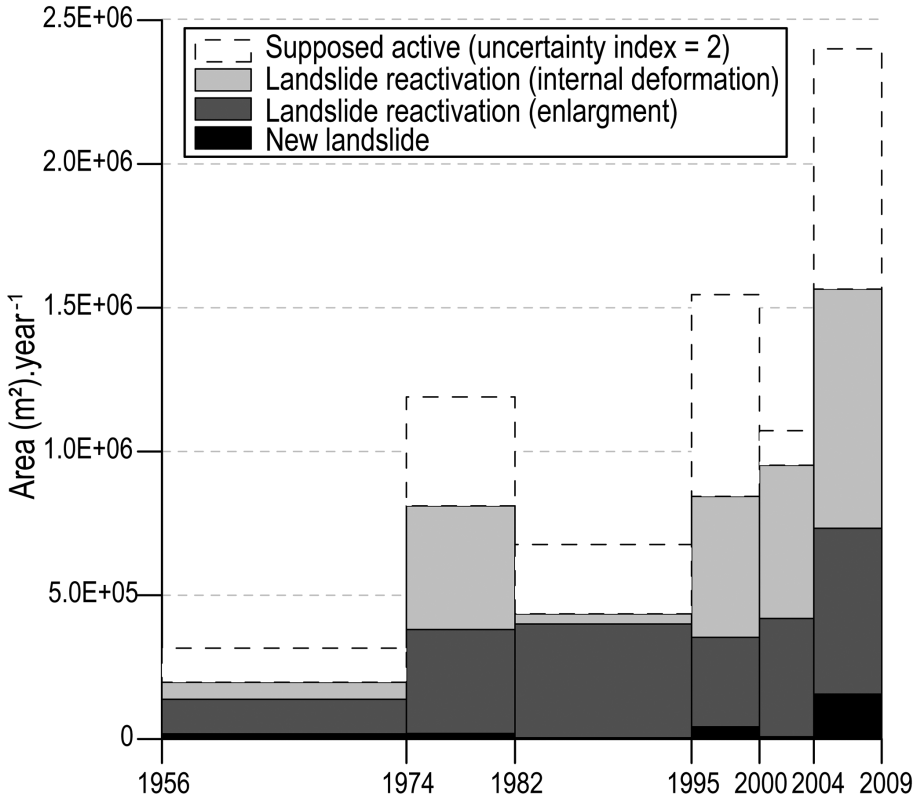

Figure 14. New and reactivated landslides per year expressed in terms of landslide area. The dotted lines indicate supposed active landslides according to the uncertainty index (equal to 2) added in the attribute table.

NHESSD
3, 2051–2098, 2015

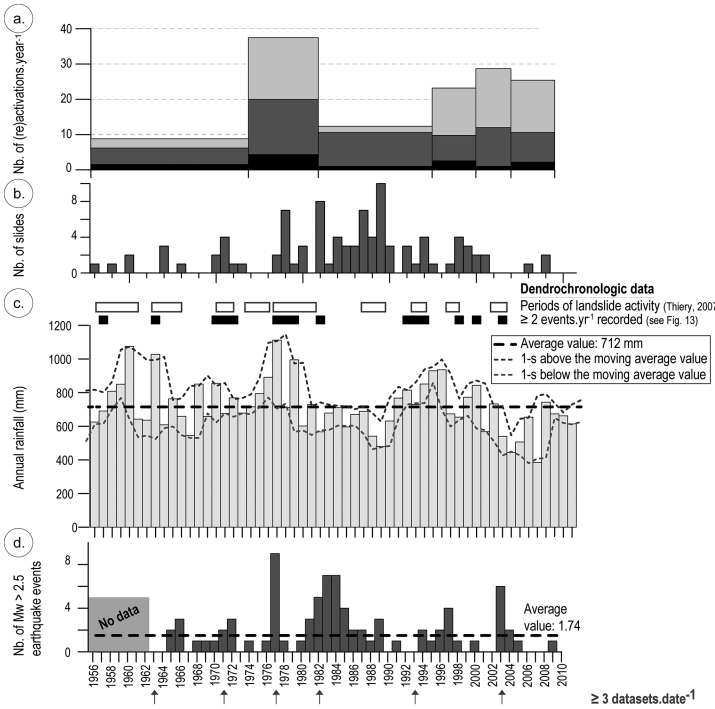

Figure 15. Relationship between the landslide periods of activity and the annual rainfall amounts for the period 1952–2012. **(a)** Number of new landslides or landslide (re)-activations from the multi-date inventory. **(b)** Number of landslides from the historical landslide catalogue of RTM/BRGM. **(c)** Periods of landslide activity recorded by dendrogeomorphological observations and relation with the annual rainfall recorded at the Barcelonnette meteorological station. Over the last 60 years, the average annual rainfall is 712 ± 152 mm. A moving average SD is plotted for 3 year periods. **(d)** Number of earthquakes with $M_w > 2.5$ within a radius of 30 km from Barcelonnette (source: SI-Hex catalogue, see Cara et al., 2014). The average yearly number of earthquakes > M_w 2.5 is 1.7.

NHESSD
3, 2051–2098, 2015